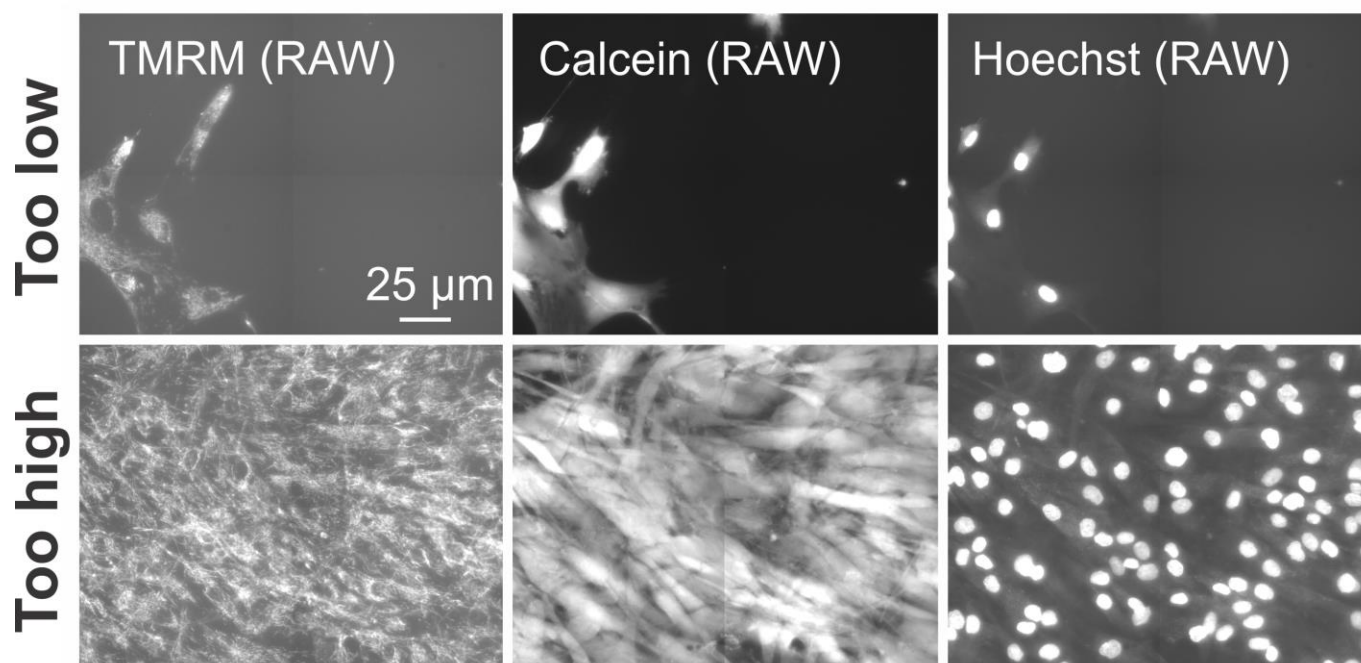


Supplementary Figure 1

Importance of the threshold (T) gray value for correct calculation of the BIN and MSK images.

(A) Typical RAW calcein image (left image) and the effect of various thresholds (numerals depict the threshold gray value) on the resulting binary (BIN) image. (B) Same as panel A but now for the RAW TMRM image of the same cells. (C) TMRM MSK image calculated using the BIN images in panel B. (D) Average value of *Casum* (total area of the objects in the calcein BIN image) and *Asum* (total area of the mitochondrial objects in the TMRM MSK image) for various threshold values. (E) Average value of *AR* (aspect ratio of mitochondrial objects), *F* (form factor: length and degree of branching of mitochondrial objects) and *Mm* (mitochondrial mass) in the TMRM MSK image for various threshold values. (F) Average value of *Dm* (mitochondrial TMRM

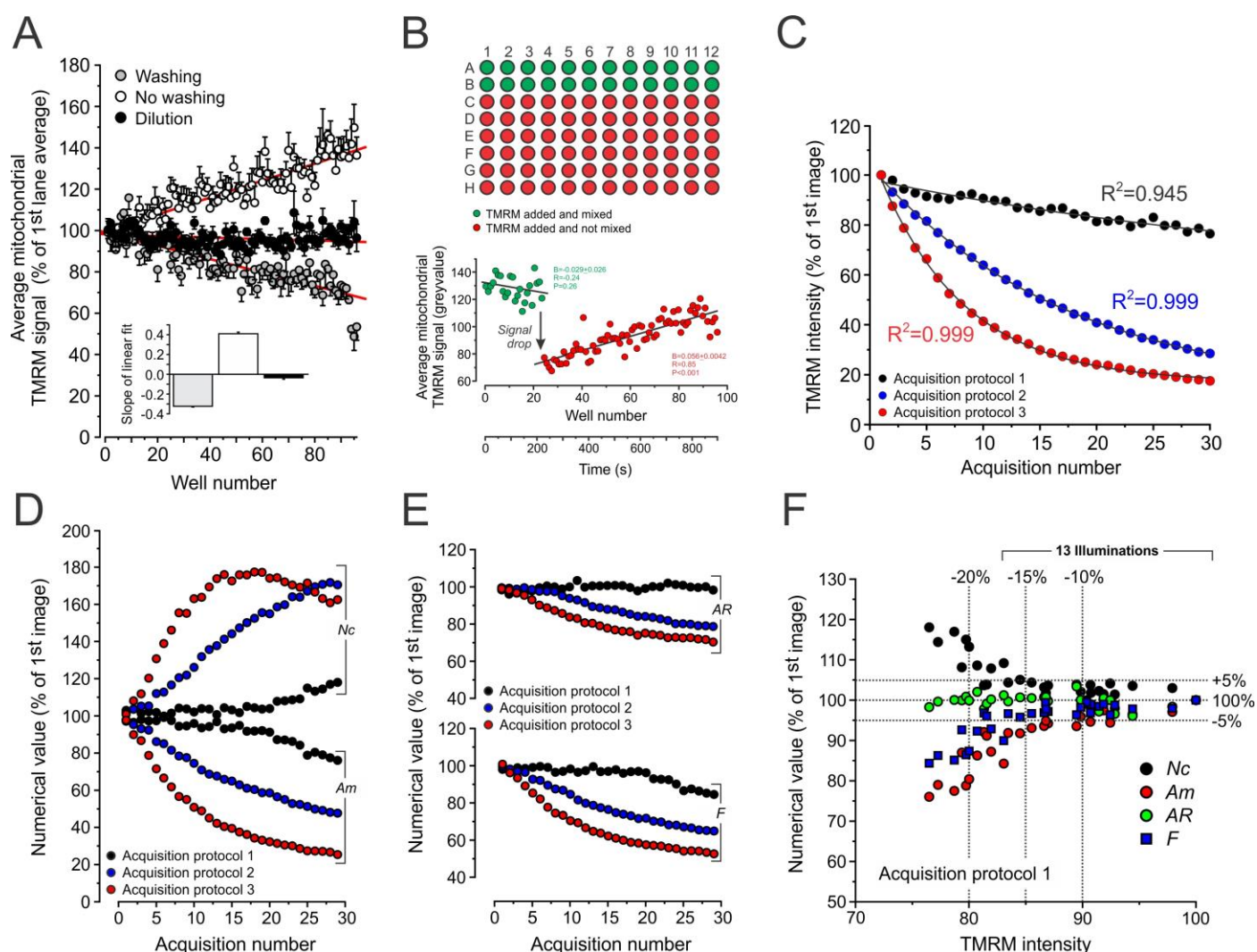
intensity in TMRM MSK image), O_t (the total number of mitochondrial objects in the TMRM MSK image), A_m (the area of individual mitochondrial objects in the TMRM MSK image) and N_c (the number of mitochondria per cell; calculated by combining information from the TMRM MSK and Hoechst BIN image) for various threshold values. Using a threshold value of 40 yielded the correct values of key descriptors between 3-6 (F), 2-3 (AR) and 50-150 (N_c), compatible with previous manual analysis (*e.g.* **Koopman et al., 2005a; Koopman et al., 2005b; Koopman et al., 2006; Koopman et al., 2008a; Distelmaier et al., 2008; Distelmaier et al., 2012; Distelmaier et al., 2015**).



Supplementary Figure 2

Illustration of too low and too high cell density.

Since images are automatically acquired for each well there is no user-control regarding which cells are imaged. Although this strategy avoids user-induced bias, it requires that the average number of imaged cells is similar between individual wells. The latter is also important to allow standardized image processing, statistical analysis and QC. This figure provides typical examples of too low and too high cell densities (relative to the proper density depicted in **Figure 5**). The protocol described in the main text was used to acquire the images in this figure.

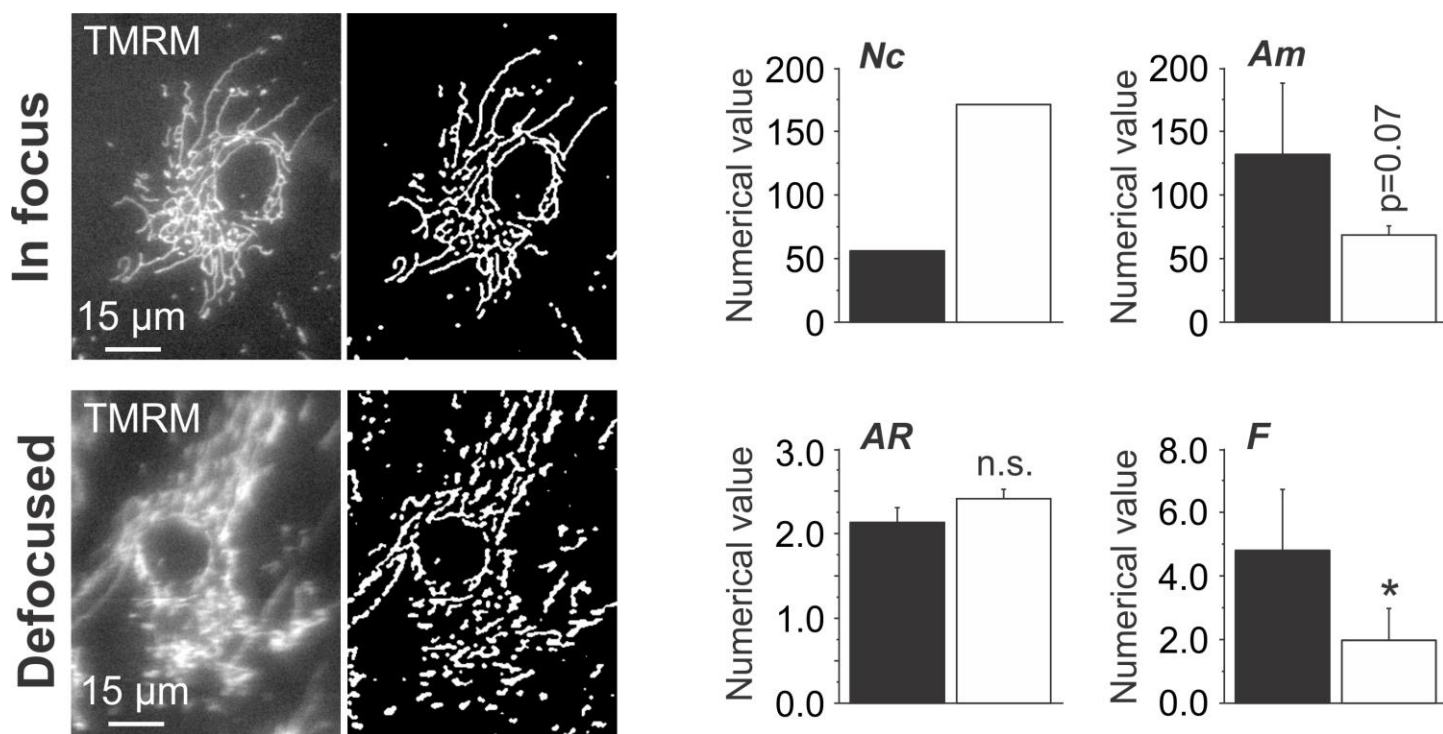


Supplementary Figure 3

Importance of the presence of extracellular TMRM, well mixing and illumination intensity for TMRM descriptor analysis.

This figure illustrates why it is important to have TMRM present outside the cell during image TMRM acquisition, why wells need to be properly mixed following TMRM addition, and the artefact-inducing effect of too high illumination intensities. Unless stated otherwise, the experimental data in this figure was acquired using the experimental protocol described in the main text. **(A)** Importance of the presence of extracellular TMRM during TMRM image acquisition. In this experiment the calcein/Hoechst loading and imaging steps were omitted. Three different manoeuvres were tested (using 5 plates/days for each condition), thereby modifying step 15 of the protocol as follows: “Washing” condition (gray symbols; two washing steps were performed using 100 μ l assay medium; 100 μ l of assay medium was present in each well during image acquisition); “No washing” condition (open symbols; nothing was done to the plate after step 13); “Dilution” condition (black symbols; 100 μ l assay medium was added to each well without washing and mixing). Only for the last condition, the fluorescence signal remained stable as indicated by the slope (inset) of a linear fit (red line). All data were normalized to the average of the first row (row A) of the plate. **Fitting results:** $P < 0.001$,

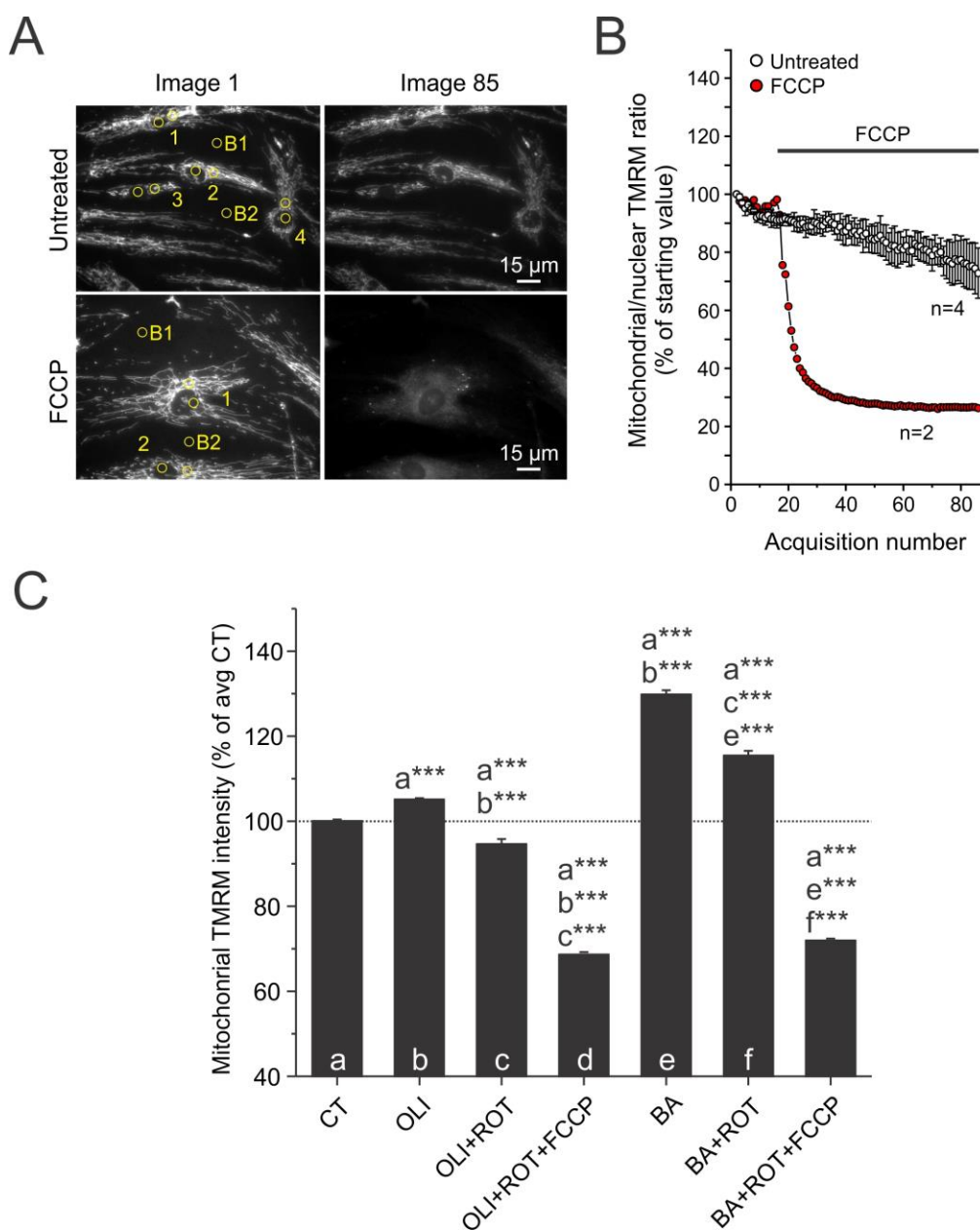
R=-0.83 (Washing condition); $P<0.001$, R=0.91 (No washing condition); $P=0.029$, R=-0.22 (Dilution condition). **(B)** Importance of mixing after TMRM addition to the well. The following steps of the protocol were modified: Step 13 (TMRM was added and mixed by pipetting up and down 4 times, but only in row A and B. For row C to H, TMRM was added but not mixed. Calcein/Hoechst staining and imaging were not required here. Only in the mixed wells (green), the TMRM signal was stable (*i.e.* the fitted line had no significant slope). **(C)** Effect of TMRM illumination intensity on the TMRM fluorescence signal. In this experiment, 30 subsequent images of the same well were acquired at the same position (Option in BD AttoVision Software: image acquisition option/acquire button/30 data points. Three different acquisition protocols were used with the following settings: Protocol 1 (Exposure time: 0.1 s; Excitation B: 548/20; Excitation dichroic: 40%; Lamp B intensity: 60%), protocol 2 (Exposure time: 0.1 s; Excitation B: 548/20; Excitation dichroic: open; Lamp B intensity: 80%), protocol 3 (Exposure time: 0.1 s; Excitation B: 548/20; Excitation dichroic: open; Lamp B intensity: 100%). Acquisition protocol 1 (used in the protocol) displayed the lowest drop in TMRM signal. **Fitting results:** TMRM intensity curves were fitted using a mono-exponential equation ($y=y_0+A_1\cdot e^{-t/\tau}$, with τ being the decay time constant). The fitted τ values equalled: 44.0 ± 23.4 (acquisition protocol 1), 17.4 ± 0.384 (acquisition protocol 2) and 7.56 ± 0.129 (acquisition protocol 3). **(D)** Effect of the three illumination protocols on the calculated mitochondrial area (Am) and number of mitochondrial objects per cell (Nc). The more the TMRM signal drops, the greater the erroneous apparent increase in Am and Nc . **(E)** Similar to panel D but now for the calculated mitochondrial aspect ratio (AR) and form factor (F). **(F)** Values of calculated key mitochondrial descriptors (Nc , Am , AR and F ; y-axis) as a function of TMRM intensity (x-axis) for acquisition protocol 1. About 13 illuminations can be carried out (*i.e.* 13 images can be acquired) before the (10-15%) drop in TMRM intensity affects descriptor quantification.



Supplementary Figure 4

Illustration of the effect of image defocusing on TMRM-reported mitochondrial morphology descriptors.

It is of the greatest importance that the acquired images are optimally focused, since defocusing will affect the extracted numerical data in a descriptor-dependent manner. This figure illustrates the effects of image defocusing on key mitochondrial descriptors. Typically, defocused images contain “artificial” small non-mitochondrial objects after image processing. The latter results in an apparent increase in the number of mitochondrial objects per cell (*Nc*), and a decrease in mitochondrial size (*Am*) and form factor (*F*). **Statistics:** Significant differences between the focused and defocused condition were assessed using an unpaired independent Student’s test and presented by: * ($P<0.05$), the actual P-value (*Am*) and by non-significant (n.s.). The protocol described in the main text was used to acquire the images in this figure.

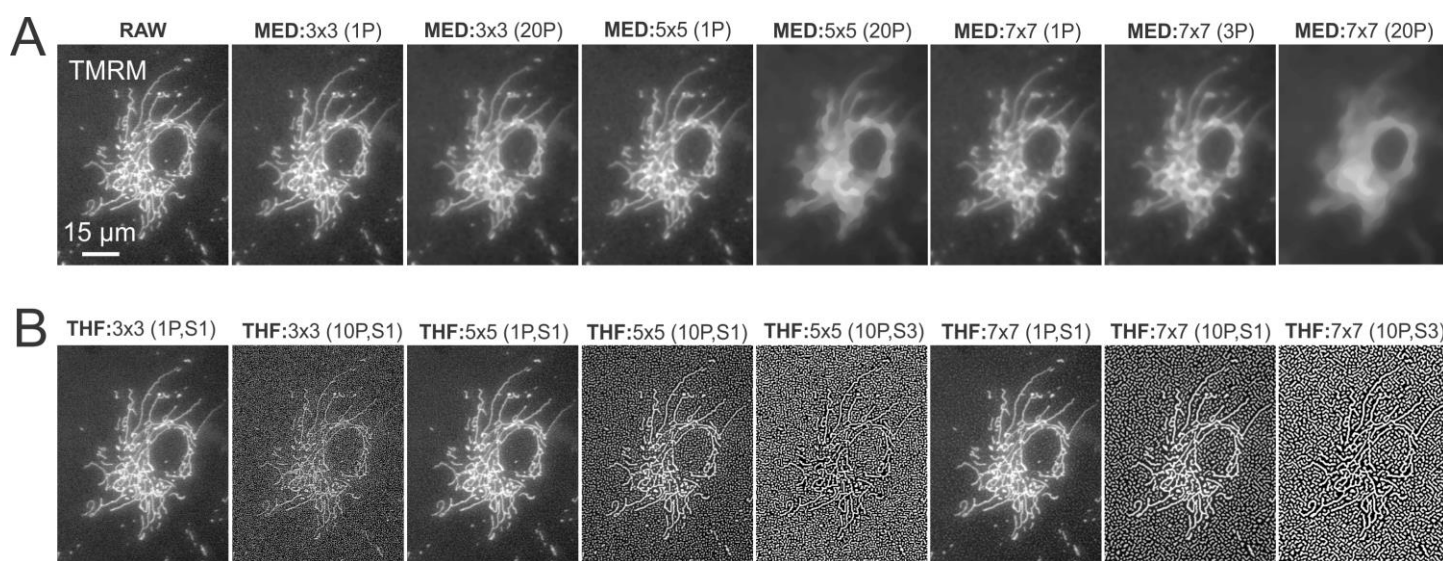


Supplementary Figure 5

Control for TMRM autoquenching, detectability of $\Delta\psi$ hyperpolarization and effect of the mitochondrial uncoupler FCCP.

This figure illustrates how to check if the TMRM fluorescence signal is affected by autoquenching and whether $\Delta\psi$ depolarization and hyperpolarization can be detected by decreased and increased mitochondrial TMRM accumulation, respectively. **(A)** Eighty-five consecutive TMRM images were acquired from the same well. The displayed typical image-pairs illustrate the effect of the mitochondrial uncoupler p-trifluoromethoxy carbonyl cyanide phenyl hydrazine (FCCP, 10 μ M; #370-86-5; Sigma-Aldrich, St. Louis, MO, USA) on mitochondrial TMRM staining (upper vs. lower panel). Numerals mark individual cells and regions of interest (ROIs; yellow) mark the nuclear and mitochondrial compartment (yellow circles). **(B)** Average ratio between TMRM intensity

in the mitochondrial and nuclear compartments calculated using the ROIs in panel A for untreated (n=4 cells) and FCCP-treated (n=2) cells. Repeated illumination induces a gradual drop in ratio (photobleaching) in the untreated cells. FCCP induces a smooth drop in the ratio signal, indicating the absence of TMRM autoquenching. If the latter would be the case, FCCP would first induce an increase in the signal (due to TMRM dequenching in the mitochondrial matrix), followed by a decrease. (C) Effect of subsequent acute addition of the F₀F₁-ATPase inhibitor Oligomycin A (OLI; 1 μ M; #1404-19-9; Sigma-Aldrich), the mitochondrial complex I inhibitor Rotenone (ROT; 1 μ M; #83-79-4; Sigma-Aldrich) and FCCP (10 μ M) on mitochondrial TMRM fluorescence intensity. In a second type of experiment, Bongkreikic acid (BA; 50 μ M; #11076-19-0; Sigma-Aldrich) was acutely added to inhibit the electrogenic mitochondrial ATP/ADP translocator (ANT). This was followed by subsequent addition of ROT and FCCP. **Statistics:** Significant differences with the indicated columns (a,b,c,d,e,f) was assessed using an unpaired independent Student's test (Origin Pro 6.1) and presented by: *** (P<0.001). **Experimental details:** Options used in the BD attovision software: "*Montage Capture Setup*", "*INACTIVE MONTAGE*", "*1 Frame*". MACRO on BD attovision software: Experiment 1 (30 (CT) TMRM image acquisitions of the same well; 30 s pause during which 1 μ M Oligomycin (OLI) is added by pipetting; 30 TMRM image acquisitions of the same well; 30 s pause during which 1 μ M Rotenone (ROT) is added; 30 TMRM image acquisitions of the same well; 30 s pause during which 10 μ M FCCP is added; 30 TMRM image acquisitions of the same well); Experiment 2 (30 (CT) TMRM image acquisitions of the same well; 30 s pause during which 50 μ M Bongkreikic acid (BA) is added; 30 TMRM image acquisitions of the same well; 30 s pause during which 1 μ M Rotenone (ROT) is added; 30 TMRM image acquisitions of the same well; 30 s pause during with 10 μ M FCCP is added; 30 TMRM image acquisitions of the same well). **Remarks:** Care should be taken that during addition of the inhibitors the pipette tip does not touch the plate to avoid altering the field of view. Inhibitors are added at twice their final concentration in a (relatively large) volume of 100 μ l to each well (which contains 100 μ l of fluid). This ensures complete and rapid mixing.



Supplementary Figure 6

Visualization of the effect of median (MED) and top-hat (THF) spatial filtering on the TMRM image.

Proper use of the MED and THF filters to reduce noise and isolate mitochondrial objects, respectively, is crucial for proper subsequent calculation of the binary image (BIN). The latter image represents white mitochondrial objects on a black background (for the complete processing pipeline see **Fig. 5C**). In this protocol, we have established the correct size of the MED and THF filter, how often they should be applied (“passes”) and, in case of the THF filter, its strength (“S”). For details about these parameters see the information in **Box 1** provided in the main text. **(A)** Effect of various MED filter settings on the TMRM image (RAW). **(B)** Effect of various THF filter settings on the TMRM image (RAW).

Supplementary Table 1 | Use of the quantification protocol in various cell types

Cell type	Staining	Imaging	Descriptors	Reference
BGM	mtEYFP	V-CLSM	<i>Am, AR, F, Nc, Mm</i>	Tronstad et al., 2014
CE	mtGFP	CLSM	<i>AR, F</i>	Hoffmann et al., 2009
CV1-4A	mtDsRed1	EPIF	<i>Am, AR, Nc</i>	De Vos et al., 2005
CHO	R123	EPIF	<i>F, Nc</i>	Distelmaier et al., 2012
Clone 9	mtRFP/mtGFP	EPIF	<i>AR, F</i>	Hom et al., 2007
COS-7	MTDR/mtGFP	EPIF	<i>AR, F</i>	Buhlman et al., 2014
CPA	TMRM	CLSM	<i>Am, AR, F, Fi</i>	Matthews et al., 2010
CPH	TMRM	CLSM	<i>Am, AR, F, Fi</i>	Matthews et al., 2010
H9c2	mtRFP	EPIF	<i>AR, F</i>	Yu et al., 2006
H9c2	MTR	EPIF	<i>AR, F</i>	Yu et al., 2008
HEK293	MTR	V-CLSM	<i>F, Nc</i>	Vogel et al., 2007
HeLa	R123	V-CLSM	<i>F, Nc</i>	Distelmaier et al., 2012
HPM	R123	V-CLSM	<i>AR, F, Nc</i>	Eisenberg et al., 2008
HUVECs	MTG	EPIF	<i>AR, F</i>	Lugus et al., 2011
HUVECs	mtGFP	CLSM	<i>Am, F, Nc, Pm</i>	Nikolaisen et al., 2014
M17HN	mtDsRed2	CLSM	<i>AR</i>	Wang et al., 2012b
MEFs	TMRM	EPIF	<i>F, Nc, Fi</i>	Distelmaier et al., 2012
MEFs	TMRM	EPIF	<i>Am, F, Mm, Nc</i>	Heeman et al., 2011
MM	Mt-roGFP2	EPIF	<i>F</i>	Cunniff et al., 2013
MPM	MTR	V-CLSM	<i>Am, AR, F, Nc, Mm</i>	Tronstad et al., 2014
N2a	R123	V-CLSM	<i>AR, F, Nc</i>	Coussee et al., 2011
PHSF	R123	V-CLSM	<i>AR, F, Fi, Nc, F/Nc</i>	Koopman et al., 2005a
PHSF	R123	V-CLSM	<i>AR, F, Nc</i>	Koopman et al., 2005b
PHSF	R123	V-CLSM	13 different	Koopman et al., 2006
PHSF	TMRM	EPIF	<i>Am, F, Fi, Nc</i>	Komen et al., 2007
PHSF	mtEYFP	V-CLSM	<i>F, Nc</i>	Koopman et al., 2007b
PHSF	mtGFP/TMRM	EPIF	<i>Fi</i>	Distelmaier et al., 2008
PHSF	TMRM	EPIF	<i>Fi</i>	Hoefs et al., 2008
PHSF	mtGFP/TMRM	EPIF	<i>Am, AR, F, Fi, Lm, Mm, Nc, Wm</i>	Koopman et al., 2008a
PHSF	R123	V-CLSM	<i>AR, F, Nc</i>	Mortiboys et al., 2008
PHSF	TMRM	EPIF	<i>Fi</i>	Distelmaier et al., 2009
PHSF	R123	V-CLSM	<i>F, Nc</i>	Willems et al., 2009
PHSF	MTG	EPIF	<i>AR, F</i>	Burbulla et al., 2010
PHSF	TMRM	EPIF	<i>AR, F, Fi, Nc</i>	Jonckheere et al., 2011
PHSF	TMRM	EPIF	<i>Am, F</i>	Baracca et al., 2013
PHSF	MTG	EPIF	<i>Am, AR, F</i>	Grau et al., 2013
PHSF	TMRM	EPIF	<i>F, Nc</i>	Szkarczyk et al., 2013
PHSF	TMRM	EPIF	<i>Am, AR, F, Fi, Mm, Nc</i>	Szkarczyk et al., 2013
PHSF	TMRM	EPIF	<i>Am, AR, F, Nc</i>	Willems et al., 2013
PHSF	TMRM/CM-H ₂ DCF	EPIF	<i>Am, AR, F, Nc, Ac</i>	Distelmaier et al., 2015
PHSF	TMRM	EPIF	31 different	Blanchet et al., 2015
PMMF	R123	V-CLSM	<i>Am, F, Nc</i>	Valsecchi et al., 2013
PMSF	R123	V-CLSM	<i>Am, F, Nc</i>	Valsecchi et al., 2013
RPAC	R123	V-CLSM	<i>Am, AR, F, Nc, Mm</i>	Tronstad et al., 2014
SH-SY5Y	mtDsRed1	EPIF	<i>AR, F</i>	Burbulla et al., 2010
SH-SY5Y	MtDsRed2	CLSM	<i>AR</i>	Wang et al., 2011
SH-SY5Y	MtDsRed2	CLSM	<i>AR</i>	Wang et al., 2012a

Abbreviations: *Ac*, area of cell; *Am*, area of mitochondrial object; *AR*, aspect ratio of mitochondrial object; BGM, Buffalo Green Monkey kidney cells; CE, intact *C. elegans*; CHO, Chinese Hamster Ovary cells; Clone9, Rat liver cells; CLSM, Confocal Laser Scanning Microscopy; CM-H₂DCF, 5-(and-6)-chloromethyl-2',7'-dichlorodihydrofluorescein; COS-7, African green monkey kidney cells; CPA, Chicken Primary Astrocytes; CPH, Chicken Primary Hepatocytes; H9c2, Rat heart myoblasts; HEK293, Human Embryonic Kidney cells; HeLa, Human epitheloid cervix carcinoma; HPM, Human Primary Myoblasts; HUVECs, Human Umbilical Vein Endothelial Cells; *Lm*, length of mitochondrial object; M17HN, M17 Human Neuroblastoma; MEFs, Mouse Embryonic Fibroblasts; *Mm*, mitochondrial mass; MM, Malignant Mesothelioma cells; MPM, Mouse Primary Myoblasts; MTDR, Mitotracker Deep Red; mtEYFP, mitochondria-targeted Enhanced Yellow Fluorescent Protein; MTG, Mitotracker Green; mtGFP, mitochondria-targeted Green Fluorescent Protein; MTR, Mitotracker Red CMXRos; MtrFP, mitochondria-targeted Red Fluorescent Protein; Mt-roGFP2, mitochondria-targeted redox-sensitive GFP2; N2a, Mouse Neuroblastoma cells; *Nc*, number of mitochondrial objects per cell; PHSF, Primary Human Skin Fibroblasts; *Pm*, perimeter of mitochondrial object; PMMF, Primary Mouse Muscle-derived Fibroblasts; PMSF, Primary Mouse Skin-derived Fibroblasts; R123, rhodamine 123; RPAC, Rat Primary Pancreatic Acinar Cells; SH-SY5Y, Human neuroblastoma cells; TMRM, tetramethyl rhodamine methyl ester; V-CLSM, Videorate Confocal Laser Scanning Microscopy; *Wm*, width of mitochondrial object. This table was adapted from: [Tronstad et al., 2014](#).

Supplementary Table 2 | Composition of the used media

CULTURE MEDIUM		ASSAY MEDIUM	
Components	mM	Components	mM
Amino Acids		Amino Acids	
Glycine	0.66667	Glycine	0.66667
L-Alanine	0.28090	L-Alanine	0.28090
L-Arginine hydrochloride	0.33175	L-Arginine hydrochloride	0.33175
L-Aspartic acid	0.22556	L-Aspartic acid	0.22556
L-Cysteine hydrochloride-H ₂ O	0.00057	L-Cysteine hydrochloride-H ₂ O	0.00057
L-Cystine 2HCl	0.10833	L-Cystine 2HCl	0.10833
L-Glutamic Acid	0.51020	L-Glutamic Acid	0.51020
L-Glutamine	0.68493	L-Glutamine	0.68493
L-Histidine hydrochloride-H ₂ O	0.10419	L-Histidine hydrochloride-H ₂ O	0.10419
L-Hydroxyproline	0.07634	L-Hydroxyproline	0.07634
L-Isoleucine	0.30534	L-Isoleucine	0.30534
L-Leucine	0.45802	L-Leucine	0.45802
L-Lysine hydrochloride	0.38251	L-Lysine hydrochloride	0.38251
L-Methionine	0.10067	L-Methionine	0.10067
L-Phenylalanine	0.15152	L-Phenylalanine	0.15152
L-Proline	0.34783	L-Proline	0.34783
L-Serine	0.23810	L-Serine	0.23810
L-Threonine	0.25210	L-Threonine	0.25210
L-Tryptophan	0.04902	L-Tryptophan	0.04902
L-Tyrosine disodium salt dihydrate	0.22222	L-Tyrosine disodium salt dihydrate	0.22222
L-Valine	0.21368	L-Valine	0.21368
Vitamins		Vitamins	
Alpha-tocopherol Phosphate	0.00001	Alpha-tocopherol Phosphate	0.00001
Ascorbic Acid	0.00028	Ascorbic Acid	0.00028
Biotin	0.00004	Biotin	0.00004
Choline chloride	0.00357	Choline chloride	0.00357
D-Calcium pantothenate	0.00002	D-Calcium pantothenate	0.00002
Folic Acid	0.00002	Folic Acid	0.00002
Menadione (Vitamin K3)	0.00006	Menadione (Vitamin K3)	0.00006
Niacinamide	0.00020	Niacinamide	0.00020
Nicotinic acid (Niacin)	0.00020	Nicotinic acid (Niacin)	0.00020
Para-Aminobenzoic Acid	0.00036	Para-Aminobenzoic Acid	0.00036
Pyridoxal hydrochloride	0.00012	Pyridoxal hydrochloride	0.00012
Pyridoxine hydrochloride	0.00012	Pyridoxine hydrochloride	0.00012
Riboflavin	0.00003	Riboflavin	0.00003
Thiamine hydrochloride	0.00003	Thiamine hydrochloride	0.00003
Vitamin A (acetate)	0.00030	Vitamin A (acetate)	0.00030

Vitamin D2 (Calciferol)	0.00025	Vitamin D2 (Calciferol)	0.00025
i-Inositol	0.00028	i-Inositol	0.00028
Inorganic Salts		Inorganic Salts	
Calcium Chloride (CaCl ₂) (anhyd.)	1.80180	Calcium Chloride (CaCl ₂) (anhyd.)	1.80180
Ferric nitrate (Fe(NO ₃)-9H ₂ O)	0.00173	Ferric nitrate (Fe(NO ₃)-9H ₂ O)	0.00173
Magnesium Sulfate (MgSO ₄) (anhyd.)	0.81392	Magnesium Sulfate (MgSO ₄) (anhyd.)	0.81392
Potassium Chloride (KCl)	5.33333	Potassium Chloride (KCl)	5.33333
Sodium Bicarbonate (NaHCO ₃)	26.1904	Sodium Bicarbonate (NaHCO ₃)	26.1904
Sodium Chloride (NaCl)	105.172	Sodium Chloride (NaCl)	117.241
Sodium Phosphate monobasic (NaH ₂ PO ₄)	1.01449	Sodium Phosphate monobasic (NaH ₂ PO ₄)	1.01449
Other Components		Other Components	
2-deoxy-D-ribose	0.00373	2-deoxy-D-ribose	0.00373
Adenine sulfate	0.02475	Adenine sulfate	0.02475
Adenosine 5'-phosphate	0.00058	Adenosine 5'-phosphate	0.00058
Adenosine 5'-triphosphate	0.00165	Adenosine 5'-triphosphate	0.00165
Cholesterol	0.00052	Cholesterol	0.00052
D-Glucose (Dextrose)	5.55556	D-Glucose (Dextrose)	5.55556
Glutathione (reduced)	0.00016	Glutathione (reduced)	0.00016
Guanine hydrochloride	0.00160	Guanine hydrochloride	0.00160
HEPES	25.0420	HEPES (add yourself)	25.0420
Hypoxanthine Na	0.00294	Hypoxanthine Na	0.00294
Phenol Red	0.05313	Phenol Red	0.0
Ribose	0.00333	Ribose	0.00333
Sodium Acetate	0.60976	Sodium Acetate	0.60976
Thymine	0.00238	Thymine	0.00238
Tween 80®	Infinity	Tween 80®	Infinity
Uracil	0.00268	Uracil	0.00268
Xanthine-Na	0.00224	Xanthine-Na	0.00224

Culture medium: Cells were cultured in culture medium (Medium 199, HEPES; #12340-030, Invitrogen, Breda, The Netherlands). To the culture medium was added: 10% (v/v) fetal calf serum (FBS; #758093, Greiner Bio-One, GmbH, Germany), 100 IU/ml penicillin and 100 IU/ml streptomycin (#30-002-CI, Corning, NY, USA).

Assay medium: TMRM, Calcein-AM and Hoechst 33258 were diluted in assay medium (Medium 199, no phenol red; #11043-023; Invitrogen, Breda, The Netherlands). To the assay medium was added: 25 mM HEPES (HEPES (1M); #15630-08, Invitrogen, Breda, The Netherlands). Washing steps were done with the assay medium; images were acquired in the assay medium.

Supplementary Table 3 | Detailed BD Pathway® 855 settings

96 WELL PLATE GREINER 655090 CELLSTAR® 96W Microplate

Setting	Calcein	Hoechst 33258	TMRM
Geometry setup			
Objective	40x Olympus	40x Olympus	40x Olympus
Ring value	0.17	0.17	0.17
Binning	1x1=0.156617µm/pixel	1x1=0.156617µm/pixel	1x1=0.156617µm/pixel
Light path			
Lamp A Transmittance	100%	100%	n.a.
Lamp B Transmittance	n.a.	n.a.	60%
Excitation A	488/10	380/10	n.a.
Excitation B	n.a.	n.a.	548/20
Excitation Dichroic	OPEN	OPEN	40%B
Emission	FURA/FITC	400DCLP	FURA/TRITC
Epifluorescence dichroic	515LP	435LP	FURA/TRITC
Auto-focus settings			
LaserAutofocus	x	x	x
Offset	1.0	1.0	1.0
Gain	40	40	40
Z-axis Relative Displacement	100 µm	100 µm	100 µm
Data points	2000	2000	2000
Sampling Rate	12000 Hz	12000 Hz	12000 Hz
Algorithm type	Double threshold	Double threshold	Double threshold
Use Rolling average	On	On	On
Rolling average size	20	20	20
Montage Capture Setup			
Active	x (4 frames)	x (4 frames)	x (4 frames)
Frames width	2	2	2
Frames height	2	2	2
Use laser autofocus during capture every 4 frames starting at frame 1	x	x	x
Dye setup			
Numerator	Exposure 0.015s	Exposure 0.01s	Exposure 0.1s
Gain	0	0	0
Offset	255	255	255
Exposure mode	Capture=on	Capture=on	Capture=on
Dynamic range	200-4095	200-4095	140-3000
Wavelength	Light path = Calcein	Light path = Hoechst	Light path = TMRM
Macro:	Calcein+Hoechst	Calcein+Hoechst	TMRM
Z-position	~5200	~5200	~5200

&Neutral density filters; % indicates the transmission from lamp A and B. Filters are denoted by their center wavelength and bandwidth (*e.g.* 470/40 = center wavelength=470 nm, bandwidth=40 nm (*i.e.* ±20 nm). **Abbreviations:** N.a. Not appropriate; ND, neutral density.

SUPPLEMENTARY REFERENCES

1. Barraca, A., Sgarbi, G., Padula, A. & Solaini, G. Glucose plays a main role in human fibroblasts adaptation to hypoxia. *Int. J. Biochem. Cell Biol.* **45**, 1356-1365 (2013).
2. Blanchet L. *et al.* Analysis of small molecule phenotypic effects using combined mitochondrial morpho-functional fingerprinting and machine learning. *Sci. Rep.* **5**, 8035 (2015).
3. Buhlman, L. *et al.* Functional interplay between Parkin and Drp1 in mitochondrial fission and clearance. *Biochim. Biophys. Acta* **1843**, 2012-2026 (2014).
4. Burbulla, L.F. *et al.* Dissecting the role of the mitochondrial chaperone mortalin in Parkinson's disease: functional impact of disease-related variants on mitochondrial homeostasis. *Hum. Mol. Genet.* **19**, 4437-4452 (2010).
5. Coussee, E. *et al.* G37R SOD1 mutant alters mitochondrial complex I activity, Ca^{2+} uptake and ATP production. *Cell Calcium* **49**, 217-225 (2011).
6. Cunliffe, B. *et al.* Mitochondrial-targeted nitroxides disrupt mitochondrial architecture and inhibit expression of peroxiredoxin 3 and FOXM1 in malignant mesothelioma cells. *J. Cell. Physiol.* **228**, 838-845 (2013).
7. De Vos K.J., Allan, V.J., Grierson, A.J. & Sheetz MP. Mitochondrial function and actin regulate dynamin-related protein 1-dependent mitochondrial fission. *Curr. Biol.* **15**, 678-683 (2005).
8. Distelmaier, F. *et al.* Mitochondrial dysfunction in primary human fibroblasts triggers an adaptive cell survival program that requires AMPK- α . *Biochim. Biophys. Acta* **1852**, 529-540 (2015).
9. Distelmaier, F. *et al.* Trolox-sensitive ROS regulate mitochondrial morphology, oxidative phosphorylation and cytosolic calcium handling in healthy cells. *Antioxid. Redox Signal.* **17**, 1657-1669 (2012).
10. Distelmaier, F. *et al.* The antioxidant Trolox restores mitochondrial membrane potential and Ca^{2+} -stimulated ATP production in human complex I deficiency. *J. Mol. Med.* **87**, 515-522 (2009).
11. Distelmaier, F. *et al.* Life cell quantification of mitochondrial membrane potential at the single organelle level. *Cytometry A* **73**, 129-138 (2008).
12. Eisenberg, I. *et al.* Mitochondrial processes are impaired in hereditary inclusion body myopathy. *Hum. Mol. Genet.* **17**, 3663-3674 (2008).
13. Grau, T. *et al.* A novel heterozygous OPA3 mutation located in the mitochondrial target sequence results in altered steady-state levels and fragmented mitochondrial network. *J. Med. Genet.* **50**, 848-858 (2013).
14. Heeman, F. *et al.* Depletion of PINK1 affects mitochondrial metabolism, calcium homeostasis and energy maintenance. *J. Cell Sci.* **124**, 1115-1125 (2011).
15. Hoefs, S.J.G. *et al.* NDUFA2 complex I mutation leads to Leigh disease. *Am. J. Hum. Genet.* **82**, 1306-1315 (2008).
16. Hoffmann, M. *et al.* *C. elegans* ATAD-3 is essential for mitochondrial activity and development. *PLoS one* **10**, e7644 (2009).
17. Hom, J.R., Gewandter, J.S., Michael, L., Sheu, S.S. & Yoon, Y. Thapsigargin induces biphasic fragmentation of mitochondria through calcium-mediated mitochondrial fission and apoptosis. *J. Cell. Physiol.* **212**, 498-508 (2007).
18. Jonckheere, A.I. *et al.* Restoration of complex V deficiency due to a deletion in the human TMEM70 gene normalizes mitochondrial morphology. *Mitochondrion* **11**, 954-963 (2011).
19. Komen, J.C. *et al.* (2007) Phytanic acid impairs mitochondrial respiration through protonophoric action. *Cell. Mol. Life Sci.* **64**, 3271-3281 (2007).
20. Koopman W.J.H., Distelmaier, F., Esseling, J.J., Smeitink, J.A.M. & Willems, P.H.G.M. Computer-assisted live cell analysis of mitochondrial membrane potential, morphology and calcium handling. *Methods* **46**, 304-311 (2008a).

21. Koopman, W.J.H. *et al.* Partial complex I inhibition decreases mitochondrial motility and increases matrix protein diffusion as revealed by fluorescence correlation spectroscopy. *Biochim. Biophys. Acta* **1767**, 940-947 (2007b).
22. Koopman, W.J.H., Visch, H.J., Smeitink, J.A.M. & Willems, P.H.G.M. Simultaneous, quantitative measurement and automated analysis of mitochondrial morphology, mass, potential and motility in living human skin fibroblasts. *Cytometry A* **69A**, 1-12 (2006).
23. Koopman, W.J.H. *et al.* Mitochondrial network complexity and pathological decrease in complex I activity are tightly correlated in isolated human complex I deficiency. *Am. J. Physiol. Cell Physiol.* **289**, C881-C890 (2005b).
24. Koopman W.J.H. *et al.* Inhibition of complex I of the electron transport chain causes oxygen radical-mediated mitochondrial outgrowth. *Am. J. Physiol. Cell Physiol.* **288**, C1440-C1450 (2005a).
25. Lugus, J.J., Ngoh, GA, Bachschmid, M.M. & Walsh, K. Mitofusins are required for angiogenic function and modulate different signaling pathways in cultured endothelial cells. *J. Mol. Cell. Cardiol.* **51**, 885-893 (2011).
26. Matthews, G.D., Gur, N. Koopman, W.J.H., Pines, O. & Vardimon, L. A weak mitochondrial targeting sequence determines tissue-specific subcellular localization of glutamine synthetase in liver and brain cell. *J. Cell Sci.* **123**, 351-359 (2010).
27. Mortiboys, H. *et al.* Mitochondrial function and morphology are impaired in parkin mutant fibroblasts. *Ann. Neurol.* **64**, 555-565 (2008).
28. Nikolaisen, J. *et al.* Automated quantification and integrative analysis of 2D and 3D mitochondrial shape and network properties. *PLoS One* **9**, e101365 (2014).
29. Szklarczyk, R. *et al.* A mutation in the FAM36A gene, the human ortholog of COX20, impairs cytochrome *c* oxidase assembly and is associated with ataxia and muscle hypotonia. *Hum. Mol. Genet.* **22**, 656-667 (2013).
30. Tronstad, K.J. *et al.* Regulation and quantification of cellular mitochondrial morphology and content. *Curr. Pharm. Des.* **20**, 5643-5652 (2014).
31. Valsecchi, F. *et al.* Primary fibroblasts of *NDUFS4*^{-/-} mice display increased ROS levels and aberrant mitochondrial morphology. *Mitochondrion* **13**, 436-443 (2013).
32. Vogel, R.O. *et al.* Cytosolic signaling protein Ecsit also localizes to mitochondria where it interacts with chaperone NDUFAB1 and functions in complex I assembly. *Genes Dev.* **21**, 615-624 (2007).
33. Wang, X. *et al.* DLP1-dependent mitochondrial fragmentation mediates 1-methyl-4-phenylpyridinium toxicity in neurons: implications for Parkinson's disease. *Aging Cell* **10**, 807-823 (2011).
34. Wang, X. *et al.* LRRK2 regulates mitochondrial dynamics and function through direct interaction with DLP1. *Hum. Mol. Genet.* **21**, 1931-1944 (2012a).
35. Wang, X. *et al.* Parkinson's disease-associated DJ-1 mutations impair mitochondrial dynamics and cause mitochondrial dysfunction. *J. Neurochem.* **121**, 830-839 (2012b).
36. Willems, P.H.G.M. *et al.* BOLA1 is an aerobic protein that prevents mitochondrial morphology changes induced by glutathione depletion. *Antioxid. Redox Signal.* **18**, 129-138 (2013).
37. Willems, P.H.G.M., Smeitink, J.A.M. & Koopman, W.J.H. Mitochondrial dynamics in human NADH:oxidoreductase deficiency. *Int. J. Biochem. Cell Biol.* **41**, 1773-1783 (2009).
38. Yu, T., Sheu, S.S., Robotham, J.L. & Yoon, Y. Mitochondrial fission mediates high glucose-induced cell death through elevated production of reactive oxygen species. *Cardiovasc. Res.* **79**, 341-351 (2008).
39. Yu, T., Robotham, J.L. & Yoon, Y. Increased production of reactive oxygen species in hyperglycemic conditions requires dynamic change of mitochondrial morphology. *Proc. Natl. Acad. Sci. USA* **103**, 2653-2658 (2006).